AUTHOR QUERY FORM

ELSEVIER	**Journal: TECTO** **Article Number: 125022**	**Please e-mail or fax your responses and any corrections to:** **E-mail: corrections.esnl@elsevier.spitech.com** **Fax: +1 619 699 6721**

Dear Author,

Any queries or remarks that have arisen during the processing of your manuscript are listed below and highlighted by flags in the proof. Please check your proof carefully and mark all corrections at the appropriate place in the proof (e.g., by using on-screen annotation in the PDF file) or compile them in a separate list.

For correction or revision of any artwork, please consult http://www.elsevier.com/artworkinstructions.

Any queries or remarks that have arisen during the processing of your manuscript are listed below and highlighted by flags in the proof. Click on the 'Q' link to go to the location in the proof.

Location in article	Query / Remark: click on the Q link to go Please insert your reply or correction at the corresponding line in the proof
Q1	Please check the telephone number of the corresponding author, and correct if necessary.
Q2	Please provide 3–5 Research Highlights. For more information, see the Guide for Authors.
Q3	As per journal style, the format for journal titles in the reference list should be consistent. Please provide the full name of those that are abbreviated.
Q4	As per journal style, the format for journal titles in the reference list should be consistent. Please provide the full name of those that are abbreviated.
Q5	As per journal style, the format for journal titles in the reference list should be consistent. Please provide the full name of those that are abbreviated.
Q6	Please provide the volume number and page range for the bibliography in Ref. [Guéguen and Kachanov, 2010].
Q7	As per journal style, the format for journal titles in the reference list should be consistent. Please provide the full name of those that are abbreviated.

Thank you for your assistance.

Tectonophysics xxx (2010) xxx–xxx

Contents lists available at ScienceDirect

Tectonophysics

journal homepage: www.elsevier.com/locate/tecto

Influence of thermal and mechanical cracks on permeability and elastic wave velocities in a basalt from Mt. Etna volcano subjected to elevated pressure

J. Fortin [a,*], S. Stanchits [b], S. Vinciguerra [c], Y. Guéguen [a]

[a] Laboratoire de Géologie, Ecole normale supérieure, CNRS UMR 8538, 24 rue Lhomond, 75005 Paris, France
[b] GFZ German Research Centre for Geosciences, Telegrafenberg D423, 14473 Potsdam, Germany
[c] Instituto Nazionale du Geofisica e Vulcanologia, Via di Vigna Murata 605, 00143 Rome, Italy

ARTICLE INFO

Article history:
Received 12 July 2010
Received in revised form 9 September 2010
Accepted 21 September 2010
Available online xxxx

Keywords:
Elastic wave velocity
Permeability
Acoustic emission
Fracture
Basalt

ABSTRACT

We report simultaneous laboratory measurements of seismic velocities and fluid permeability on lava flow basalt from Etna (Italy). Results were obtained for dry and saturated samples deformed under triaxial compression. During each test, the effective pressure was first increased up to 190 MPa to investigate the effect of pre-existing crack closure on seismic properties. Then, the effective pressure was unloaded down to 20 MPa, a pressure which mirrors the stress field acting under a lava pile of approximately 1.5–2 km thick, and deviatoric stress was increased until failure of the specimens.
Using an effective medium model, the measured elastic wave velocities were inverted in terms of two crack densities: ρ_i the crack density of the pre-existing thermal cracks and ρ_v the crack density of the stress-induced cracks. In addition a link was established between elastic properties (elastic wave velocities V_p and V_s) and permeability using a statistical permeability model.
Our results show that the velocities increase with increasing hydrostatic pressure up to 190 MPa, due to the closure of the pre-existing thermal cracks. This is interpreted by a decrease of the crack density ρ_i from ~1 to 0.2. The effect of pre-existing cracks closure is also highlighted by the permeability evolution which decreases of more than two orders of magnitude.
Under deviatoric loading, the velocities signature is interpreted, in the first stage of the loading, by the closure of the pre-existing thermal cracks. However, with increasing deviatoric loading newly-formed vertical cracks nucleate and propagate. This is clearly seen from the velocity signature and its interpretation in term of crack density, the location of the acoustic emission sources, and from microstructural observations. This competition between pre-existing cracks closure and propagation of vertical cracks is also seen from the permeability evolution, and our study shows that mechanically-induced cracks has lesser influence on permeability change than pre-existing thermal cracks.

1. Introduction

The complex stress field acting in the area surrounding Mount Etna (Italy), the largest volcano in Europe, is generated by the combined effects of regional tectonics and transient local stresses caused by magma rising within feeder dykes. In particular, over-pressured magma stored in shallow reservoirs induces bursts of seismic activity and episodes of ground deformation that occur from years to months before a new major eruption. Over the last 20 years, new technological developments and denser monitoring networks at Mt. Etna volcano have provided one of the highest quality volcanological, geophysical and geochemical data sets for any volcano in the world, and recent pre-eruptive stages have been closely monitored by using both ground deformation and seismic arrays (Briole et al., 1990; Castellano et al., 1993; Ferrucci et al., 1993).

Improvements in seismic monitoring have resulted in interpretative models of the physical changes of the edifice and these models are based on a-priori knowledge of the changing physical and mechanical properties of the basalt. Indeed elastic wave velocities in the earth are sensitive to the in-situ stress, pore pressure, and anisotropy of the rock fabric resulting from the depositional and stress history of the rock. Thus, quantifying the physical properties, such as the elastic wave velocities and permeability, of the rocks constituting Mt. Etna volcano's edifice is of key importance in establishing the reliability of modeled deformation processes.

In the laboratory, parameters such as elastic wave velocities and permeability can be investigated under different conditions. Previous laboratory measurements on Etna basalt have focused on the effect of pre-existing thermal-induced cracks with hydrostatic pressure up to 90 MPa on the *P*- and *S*-wave velocities and permeability (Vinciguerra et al., 2005; Benson et al., 2006). More recently, the effect of the

* Corresponding author. Tel.: +33 1 44 32 2206.
E-mail address: jerome.fortin@ens.fr (J. Fortin).

0040-1951/$ – see front matter © 2010 Published by Elsevier B.V.
doi:10.1016/j.tecto.2010.09.028

deviatoric stress on the P- and S-wave velocities was investigated in dry condition, in triaxial compression experiments performed in pressure cycles at 20, 40, and 60 MPa in Stanchits et al. (2006), and the degradation of elastic moduli during cyclic stressing of samples was investigated in the study of Heap et al. (2009b).The location of acoustic emission (AE) sources during deformation of rock has proven to be a useful nondestructive analytic technique to study the formation and growth of faults (Lockner et al., 1977; Zang et al., 2000; Schubnel et al., 2003; Fortin et al., 2006). Moreover, a recent study has shown that low-frequency (AE) events, analogous to volcanic long-period seismicity, could be triggering during experimental deformation of a basalt (Benson et al., 2008; Burlini and DiToro, 2008).

In this paper, we report experimental results obtained during triaxial compression tests performed on a basalt from Mt. Etna in dry and in saturated conditions. Elastic wave velocities, porosity and permeability evolution as well as the AE were measured. A novel method to look at the separate influence of two populations of cracks – thermal and mechanical cracks – was developed. The first population exists in the undeformed specimens and is randomly oriented due to thermal cracking during formation of basalt whereas the second fabric is mechanically induced by the deviatoric loading. This second population is characterized by cracks with normal perpendicular to the axial compressive stress.

Elastic waves are, in essence, small mechanical perturbations and are therefore affected by the rock microstructure and rock deformation processes. Thus, to quantitatively interpret our velocity data we used a micromechanical model based on effective medium concepts. In the studies of Benson et al. (2006) and Schubnel et al. (2006), the elastic wave measurements obtained during hydrostatic loading were inverted in terms of crack density evolution (Walsh, 1965). In this study, the effective medium model is also based on the work of Kachanov (Kachanov, 1980, 1994; Sayers and Kachanov, 1995), but the model is generalized to consider two crack densities: ρ_i, the pre-exiting crack density (randomly oriented) and ρ_v, the vertical crack density mechanically induced. Thus, this model, when written in terms of transversely isotropic symmetry, can be applied to velocities obtained during hydrostatic loading and during deviatoric loading.

Benson et al. (2006) and Vinciguerra et al. (2005) have reported the decrease in permeability associated with increasing pressure in Etna basalt interpreted by the closure of pre-existing cracks. However, the effect of deviatoric stress on permeability is not well understood. In this study, we have also investigated the change in permeability as a function of increasing hydrostatic pressure and deviatoric stress. In addition the relation between the evolutions of the permeability and the elastic wave velocity is investigated using a statistical permeability model (Dienes, 1982; Guéguen and Dienes, 1989).

2. Experimental techniques

2.1. Sample material and testing procedure

Mt. Etna is a composite volcano made from many layered deposits. The most representative basalt from Mt. Etna volcano is a porphyritic, intermediate, alkali basalt (Tanguy et al., 1997). The samples of Etna basalt used in this study were cored from similar block as that studied by Stanchits et al. (2006) and Heap et al. (2009b). It is a lava flow basalt and the exact location of the quarry from which the block was collected can be found in Heap et al. (2009b). Experiments were performed on cylindrical samples of 50 mm diameter and 125 mm length.

Initial density and porosity were determined using a gas pycnometer (Accupyc 1330). A density of 2.76 ± 0.01 g/cm^3 and a connected porosity of 4.7% were found respectively, in agreement with previous studies (Zhu et al., 2007; Heap et al., 2009b). The specimens contain mm-sized phenocrysts of pyroxene, olivine and feldspar in a fine-grained groundmass. The grain size ranges from 0.9 mm to 1.8 mm with an average value of 1.3 mm (Stanchits et al., 2006).

The experiments were performed at the GeoForshungZentrum Potsdam. We used a servo-hydraulic frame from Material Testing Systems (mts) with a load capacity of 4600 kN (Fig. 1a). Experiments were performed on dry and wet basalt samples at room temperature. The dry sample was kept in a oven at 50 °C temperature under vacuum (~10^{-2} bar) for more than 12 h. To prepare the wet sample, the specimen was first saturated with distilled water for more than 12 h. The test was carried out at drained conditions with a mean constant pore fluid (water) pressure $P_p = 10$ MPa using Quizix pore pressure pumps.

In both experiments, two data sets were obtained. A first one, was obtained under isotropic stress condition: the effective confining pressure was increased up to 190 MPa followed by unloading down to 20 MPa. In the case of the dry experiment, the confining pressure was increased at a rate of 0.01 MPas^{-1}. In the case of the saturated experiment, confining pressure was increased in steps of 30 MPa and the pressurization ramp was 0.01 MPas^{-1}. Keeping confining pressure fixed for about 10 min during these steps was required for permeability measurements by steady flow technique.

The second data set were obtained from a triaxial load on both dry and wet samples done at 20 MPa effective confining pressure. The axial loading was displacement-controlled at a rate of 0.02 mm/min. The choice of a 20 MPa confining pressure mirrors well the low lithostatic pressure acting in the field, where the lava flows have a thickness of 1.5 − 2 km from the surface. However, hydrostatic cycles with higher pressures (up to 190 MPa) were adopted in order to investigate the effect of crack closure on the seismic properties. In addition, theses cycles are relevant to interpret field seismic velocities of intrusive basalt bodies which are cooled at depth between 5 and 10 km (Patanè et al. 2003).

2.2. AE, elastic wave velocities, strain, and permeability measurements

We use, in this study, the convention that compressive stresses and compactive strains are positive. The maximum and minimum (compressive) stresses are denoted by σ_1 and σ_3, respectively. The pore pressure is denoted by P_p, and the difference between the confining pressure (P_c) and the pore pressure is referred to as the “effective pressure”. The effective mean stress $(\sigma_1 + 2\sigma_3)/3 - P_p$ will be denoted P and the differential stress $\sigma_1 - \sigma_3$ by Q.

Acoustic emissions (AE) and elastic wave velocity changes were monitored by twelve P-wave and four S-polarized piezoelectric sensors, either embedded in the pistons or glued to the sample surface and sealed in a neoprene jacket using two-component epoxy (Fig. 1b) (Stanchits et al., 2006; Fortin et al., 2009; Stanchits et al., 2009). P- and S-wave sensors were produced from PZT piezoceramic discs with 5 mm diameter and 1 mm thickness and rectangular piezoceramic plates 5 × 5 × 1 mm, respectively. Transducer signals were amplified by 40 dB using *Physical Acoustic Corporation* pre-amplifiers. Full-waveform AE data and the ultrasonic signals for P- and S-wave velocity measurements were stored in a 12-channel transient recording system (DaxBox, Prökel, Germany) with an amplitude resolution of 16 bit at 10 mHz sampling rate. For periodic elastic wave velocity measurements, six P- and two S-sensors were used as senders applying 100 V pulses every ~30 s during the loading. Ultrasonic transmissions and AE waveforms were discriminated automatically after the experiments. Hypocenter locations were estimated using a downhill simplex algorithm considering time dependent changes of the anisotropic velocity field. AE hypocenter location errors are estimated to be ±1 mm.

Volumetric strain was estimated using two pairs of strain gages glued directly onto the sample surface. The strain gages were oriented parallel to the sample axis (ε_1) and in a circumferential direction (ε_3).

Please cite this article as: Fortin, J., et al., Influence of thermal and mechanical cracks on permeability and elastic wave velocities in a basalt from Mt. Etna volcano subjected to elevated pressure, Tectonophysics (2010), doi:10.1016/j.tecto.2010.09.028

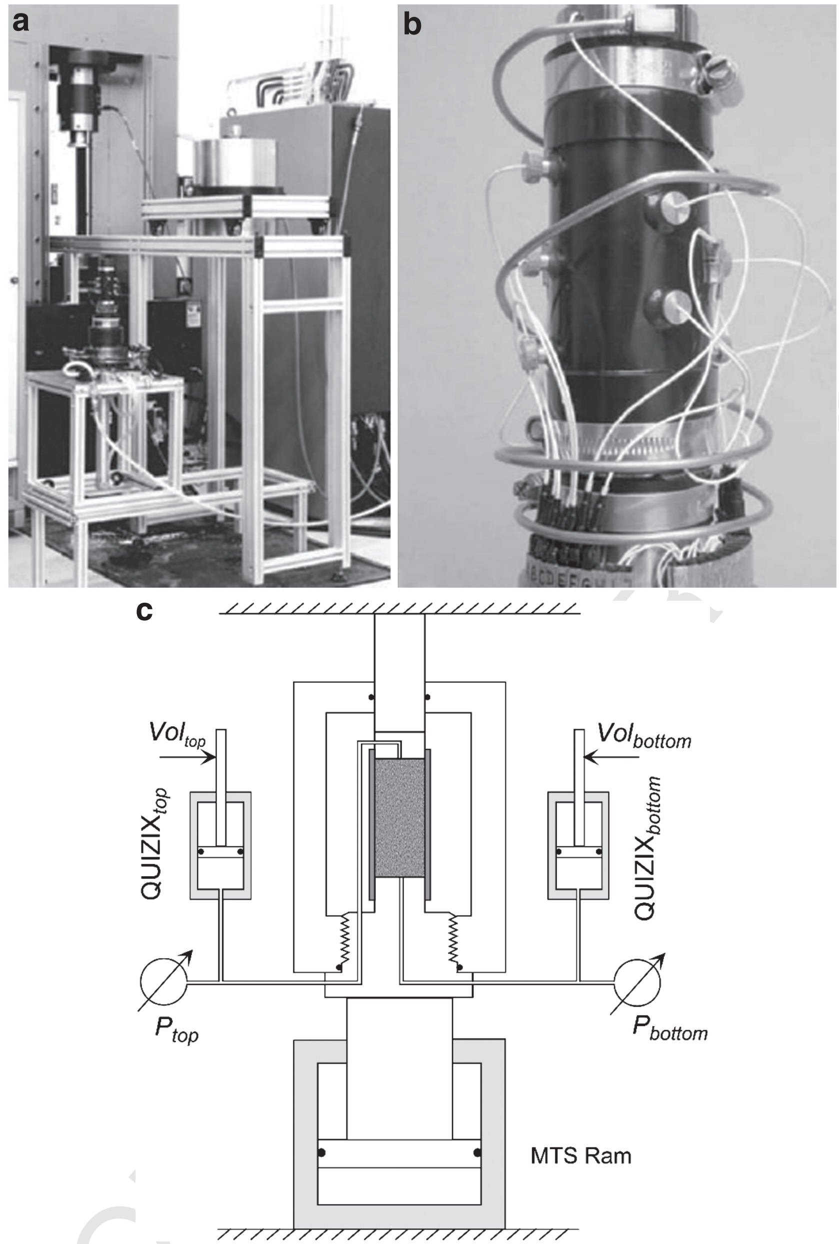

Fig. 1. Experimental setup. a) MTS loading frame with 200 MPa pressure vessel. b) Cylindrical specimen encapsulated in rubber jacket with P sensors glued directly on the sample surface. c) Schematic diagram of permeameter/volumometer used for permeability measurements.

Volumetric strain ε_v was calculated using: $\varepsilon_v = \varepsilon_1 + 2\varepsilon_3$. During axial loading axial strain, ε_1, was also measured by a linear variable differential transducer (LVDT) mounted at the end of the piston and corrected for the effective stiffness of the loading frame.

Permeability measurements were done in the wet specimen using three different techniques. Permeability measurements were first made using the steady state flow technique: a small pore pressure difference is imposed across the sample and, once steady state flow is established, permeability can be calculated from Darcy's law. These measurements were made during hydrostatic loading at fixed confining pressure and during axial loading at fixed deviatoric stress. During hydrostatic loading, the pore pressure difference across the sample was for $P_c < 0.6$ MPa $P_c < 30$ MPa and was increased gradually with increasing confining pressure (at $P_c = 185$ MPa, the pore pressure difference was 2 MPa). During axial loading, the pore pressure difference across the sample was 1.2 MPa. In addition to these measurements, permeability was also measured during hydrostatic loading for $P_c > 100$ MPa using a pulse technique following the method of Brace et al. (1968).To estimate the permeability continuously during loading, we also decided to keep a small pore pressure difference during hydrostatic loading as well as during axial loading. In this case, if we assume that the steady state of the pore fluid flow is established (which is valid if the pressurization ramp is slow enough), the change in the upstream pore fluid reservoir (Quizix top, on Fig. 1c) is:

$$\frac{\Delta Vol_{top}}{\Delta t} = \varphi + \frac{\Delta \phi}{2\Delta t}, \tag{1}$$

where t is the time, φ the flow induced by the small pore pressure difference, and $\Delta\phi$ is the volume of water expelled from the sample due to the closure of cracks and pores, i.e. the change in porosity due

Please cite this article as: Fortin, J., et al., Influence of thermal and mechanical cracks on permeability and elastic wave velocities in a basalt from Mt. Etna volcano subjected to elevated pressure, Tectonophysics (2010), doi:10.1016/j.tecto.2010.09.028

to the increase in effective pressure. Thus the change in the downstream pore fluid reservoir (Quizix bottom, on Fig. 1c) is:

$$\frac{\Delta Vol_{bottom}}{\Delta t} = -\varphi + \frac{\Delta\phi}{2\Delta t}, \tag{2}$$

Note that in Eqs. (1) and (2) we assume that the volume of water induced by an increase in effective pressure, $\Delta\phi$, expels equally into the upstream and downstream reservoirs. As a consequence, the change in porosity, $\Delta\phi$ can be directly obtained from the evolution of $Vol_{top} + Vol_{bottom}$, whereas the flow induced by the small pore pressure difference φ can be obtained from $\frac{Vol_{top} - Vol_{bottom}}{\Delta t}$. Then the permeability can be calculated from φ and Darcy's law. In this third technique, two strong assumptions are made; 1) we assume that the steady state is established, and 2) we assume that the volume of water induced by an increase in effective pressure, $\Delta\phi$, expelled equally into the upstream and downstream reservoirs.

3. Modeling elastic properties

3.1. Theoretical background

In this section, we use the convention, that $\underline{A}$ is a vector, $\underline{\underline{A}}$ is a second rank tensor and $\mathbb{A}$ a fourth rank tensor. Quantitative characterization of a microstructure in the context of effective elasticity means identification of the proper microstructural parameters (Guéguen and Kachanov, 2010). In the case of a medium containing circular cracks, a crack density parameter, ρ, can be defined as $\rho = \frac{1}{V}\sum_0^N c_i^3$, where c_i is the radius of the ith crack and N is the total number of cracks embedded in the representative volume V (Bristow, 1960; Walsh, 1965). This parameter is adequate for the isotropic case of randomly oriented cracks but cannot be used for diverse crack orientation distributions. Following the work of Kachanov (1980), the scalar crack density ρ can be generalized to a second crack density tensor, $\underline{\underline{\alpha}}$, defined as $\underline{\underline{\alpha}} = \frac{1}{V}\sum_0^N (c^3\underline{n} \otimes \underline{n})_i$, where $\underline{n}$ is the unit normal to a crack, and $\underline{n} \otimes \underline{n}$ is the dyadic product. Note that the linear invariant $\mathrm{tr}(\underline{\underline{\alpha}}) = \alpha_{kk}$ is the scalar crack density ρ.

For a medium containing cracks, the elastic potential $f(\underline{\underline{\sigma}})$ for a given tensor stress state $\underline{\underline{\sigma}}$ (from which the macroscopic volume-averaged strains are obtained as $\varepsilon_{ij} = \partial f / \partial \sigma_{ij}$) may be written as a sum:

$$f = f_o + \Delta f, \tag{3}$$

where $f_o = \frac{1}{2E_o}\left[(1+\nu_o)\mathrm{tr}(\underline{\underline{\sigma}}.\underline{\underline{\sigma}}) - \nu_o(\mathrm{tr}\underline{\underline{\sigma}})^2\right]$ is the potential of the bulk material (E_o, ν_o are its Young's modulus and Poisson's ratio), and Δf is the additional term due to the presence of cracks (Kachanov, 1994). In this approach, contributions of cracks are evaluated in the non-interaction approximation (NIA), without accounting for the interaction between cracks. This approximation has been proved to be valid up to crack density of at least 0.5 (Kachanov, 1994; Schubnel and Guéguen, 2003; Guéguen and Kachanov, 2010). The formulation of the elastic potential Δf for a solid with multiple circular cracks in arbitrary orientational distribution is given by Kachanov (1980), as:

$$\Delta f = \frac{16\left(1-\nu_o^2\right)}{3(2-\nu_o)E_o}\left(\underline{\underline{\sigma}}.\underline{\underline{\sigma}} : \underline{\underline{\alpha}} + \left[\left(1-\frac{\nu_o}{2}\right)\frac{\delta}{1+\delta} - 1\right] \underline{\underline{\sigma}} : \mathbb{B} : \underline{\underline{\sigma}}\right), \tag{4}$$

where δ is a non dimensional number referred to as the saturation parameter, and is defined by

$$\delta = \frac{9\pi(1-2\nu_o)}{16(1-\nu_o^2)}\frac{K_o}{K_f}\zeta. \tag{5}$$

K_f is the fluid bulk modulus, ζ the mean crack aspect ratio ($\zeta = \frac{w}{c}$, where w is the crack average opening), and K_o the bulk modulus on the crack-free material. The coefficient δ characterizes coupling between stresses and fluid pressures and determines the impact of fluid on the effective compliance. In the limit case of a dry medium, $K_f \to 0$, and the ratio $\frac{\delta}{1+\delta} \to 1$. The formulation of the elastic potential Δf (Eq. (4)) introduces a second crack density parameter $\mathbb{B}$, which is a fourth rank tensor, defined as $\mathbb{B} = \frac{1}{V}\sum_0^N \left(c^3\underline{n} \otimes \underline{n} \otimes \underline{n} \otimes \underline{n}\right)_i$. Finally, the extra compliance due to cracks $\underline{\underline{\Delta S}}$ can be obtained by differentiation of Eq. (4) with respect to stresses (Sayers and Kachanov, 1995).

Our particular interest is the case of transversely isotropic symmetry. Assuming x_3 as the axis of symmetry, this leads to $\alpha_{11} = \alpha_{22}$, $B_{1111} = B_{2222}$ and $B_{1212} = B_{1122} = B_{1111}/3$ (Sayers and Kachanov, 1995). The compliance, given in the Voigt (two-index) notation of a material containing cracks are:

$$S_{11} = S_{22} = \frac{1}{E_o} + h(\alpha_{11} + CB_{1111}), \tag{6}$$

$$S_{33} = \frac{1}{E_o} + h(\alpha_{33} + CB_{3333}), \tag{7}$$

$$S_{44} = \frac{1}{G_o} + h(\alpha_{11} + \alpha_{33} + 4CB_{1133}), \tag{8}$$

$$S_{66} = \frac{1}{G_o} + h(2\alpha_{11} + 4/3CB_{1111}), \tag{9}$$

$$S_{12} = -\frac{\nu_o}{E_o} + h(1/3CB_{1111}), \tag{10}$$

$$S_{13} = S_{23} = -\frac{\nu_o}{E_o} + h(CB_{1133}), \tag{11}$$

$$\text{with} \quad C = \left[\left(1-\frac{\nu_o}{2}\right)\frac{\delta}{1+\delta} - 1\right] \tag{12}$$

where G_o is the shear modulus on the crack-free material and the scalar $h = \frac{32\left(1-\nu_o^2\right)}{3(2-\nu_o)E_o}$.

The Eqs. ((6) to (12)) are valid, in the case of transversely isotropic symmetry, for any arbitrary distributions of cracks. In the case of our experiments, we can assume that two populations of cracks are present. A first one, present in the undeformed specimens due to thermal cracking during formation of basalt. This population is characterized by cracks randomly oriented (LeRavalec and Guéguen, 1994). The second population is characterized by cracks with normals randomly oriented within planes parallel to the (x_1,x_2) plane. This orientation distribution is expected to approximate the micro-cracks distribution which results when increasing axial compressive stress is applied in the Ox_3 direction.

Considering a medium containing these two populations of cracks, Eq. (3), can be re-written in the NIA assumption as follows:

$$f = f_o + \Delta f_i + \Delta f_v, \tag{13}$$

where Δf_i is the additional term due to the presence of cracks randomly oriented, characterized by a crack density ρ_i and a mean aspect ratio ζ_i ; and Δf_v is the additional term due to the presence of vertical cracks, characterized by a crack density ρ_v and a mean aspect ratio ζ_v.

The compliance for a medium containing randomly oriented cracks can be obtained from Eqs. ((6) to (12)), with $\alpha_{11} = \alpha_{22} = \alpha_{33} = \frac{\rho_i}{3}$, where ρ_i is the randomly oriented crack density, and $B_{1111} = B_{3333} = 3B_{1133} = \rho_i/5$. The compliance for a medium containing vertical cracks with normals randomly oriented within planes parallel to the (x_1,x_2) plane can be obtained from Eqs. ((6) to (12)), with $\alpha_{33} = 0$, and $\alpha_{11} = \alpha_{22} = \frac{\rho_v}{2}$, where ρ_v is the vertical crack density, and in this

Please cite this article as: Fortin, J., et al., Influence of thermal and mechanical cracks on permeability and elastic wave velocities in a basalt from Mt. Etna volcano subjected to elevated pressure, Tectonophysics (2010), doi:10.1016/j.tecto.2010.09.028

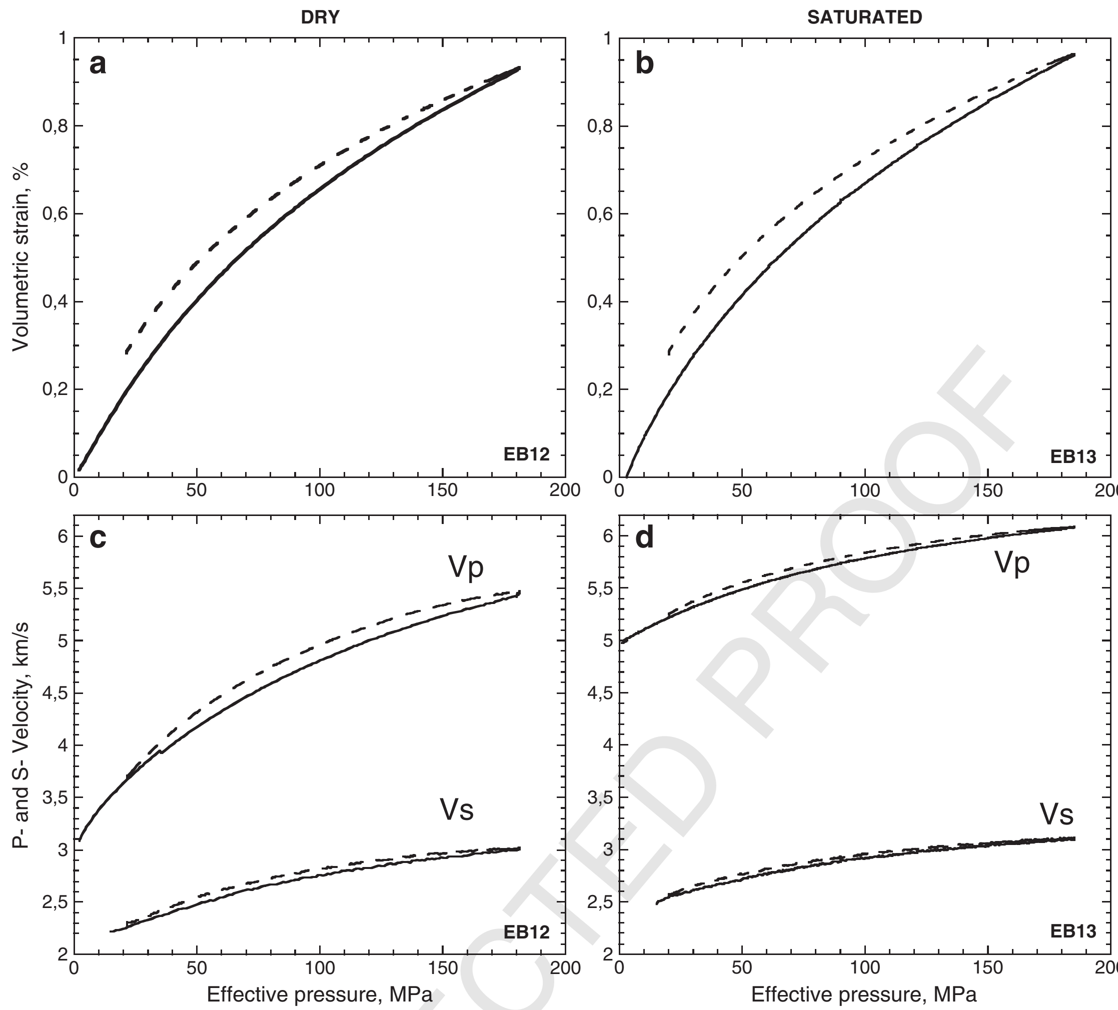

Fig. 2. Mechanical data and velocity measurements for the hydrostatic loading on sample EB12 done in dry condition and on sample EB13 done in saturated condition. (a) and (b) Volumetric strain versus effective confining pressure. (c) and (d) *P* and *S* wave velocities versus effective confining pressure. Unloading is plotted as dashed lines.

particular case, we can calculate the components of $\mathbb{B}$, and $B_{1111} = 3/8\rho_v$ and $B_{3333} = B_{1133} = 0$. Finally, according to Eq. (13), the compliance for a material containing a population of randomly oriented cracks, and a population of vertical cracks are:

$$S_{11} = S_{22} = \frac{1}{E_o} + \rho_i h/3(1 + 3/5C_i) + \rho_v h/2(1 + 3/4C_v), \quad (14)$$

$$S_{33} = \frac{1}{E_o} + \rho_i h/3(1 + 3/5C_i), \quad (15)$$

$$S_{44} = \frac{1}{G_o} + \rho_i h2/3(1 + 2/5C_i) + \rho_v h/2, \quad (16)$$

$$S_{66} = \frac{1}{G_o} + \rho_i h2/3(1 + 2/5C_i) + \rho_v h(1 + 1/4C_v), \quad (17)$$

$$S_{12} = -\frac{\nu_o}{E_o} + \rho_i h/15C_i, + \rho_v h/8C_v, \quad (18)$$

$$S_{13} = S_{23} = -\frac{\nu_o}{E_o} + \rho_i h/15C_i, \quad (19)$$

where C_i and C_v are obtained from Eqs. ((5) and (12)) using, respectively, ζ_i and ζ_v instead of ζ.

3.2. Inversion procedure

During the experiments, elastic wave measurements are made at a given loading stage. From these measurements, five independent elastic wave velocities measurements are enough to determine the full current dynamic elastic tensor $\mathbb{C}$. For the inversion, we used Vp_{axial}, the *P*-velocity measured parallel to the loading (Ox_3 direction); Vp_{radial}, the *P*-velocity measured perpendicular to the loading; $Vp_{45°}$, the *P*-velocity measured at 45° to Ox_3; Vs_{vert}, and Vs_{hor} the *S*-velocities measured perpendicular to the loading, polarized in the vertical direction and in the horizontal direction, respectively (Mavko et al., 1998). Using $\mathbb{S} = \mathbb{C}^{-1}$, the experimental value of $S_{11}^{exp}; S_{33}^{exp}; S_{44}^{exp}; S_{66}^{exp}; S_{12}^{exp}$ and S_{13}^{exp}, at a given loading stage can be calculated.

Finally, the theoretical predictions of the effective medium model provided by Eqs. (14)–(19), (12) and (5), in terms of effective compliance are compared to the elastic compliance obtained from the elastic wave velocities measurements, and the distance between them is defined by a least-square function, *F*, as,

$$F = 4(S_{11}^{exp} - S_{11})^2 + 4(S_{33}^{exp} - S_{33})^2 + (S_{66}^{exp} - S_{66})^2 + (S_{44}^{exp} - S_{44})^2 + 4(S_{12}^{exp} - S_{12})^2 + 4(S_{13}^{exp} - S_{13})^2, \quad (20)$$

that need to be minimized at each loading stage. A weight is assigned to the compliances deduced from the *P*-wave velocities, which are more accurate experimental data than the compliance deduced from

Please cite this article as: Fortin, J., et al., Influence of thermal and mechanical cracks on permeability and elastic wave velocities in a basalt from Mt. Etna volcano subjected to elevated pressure, Tectonophysics (2010), doi:10.1016/j.tecto.2010.09.028

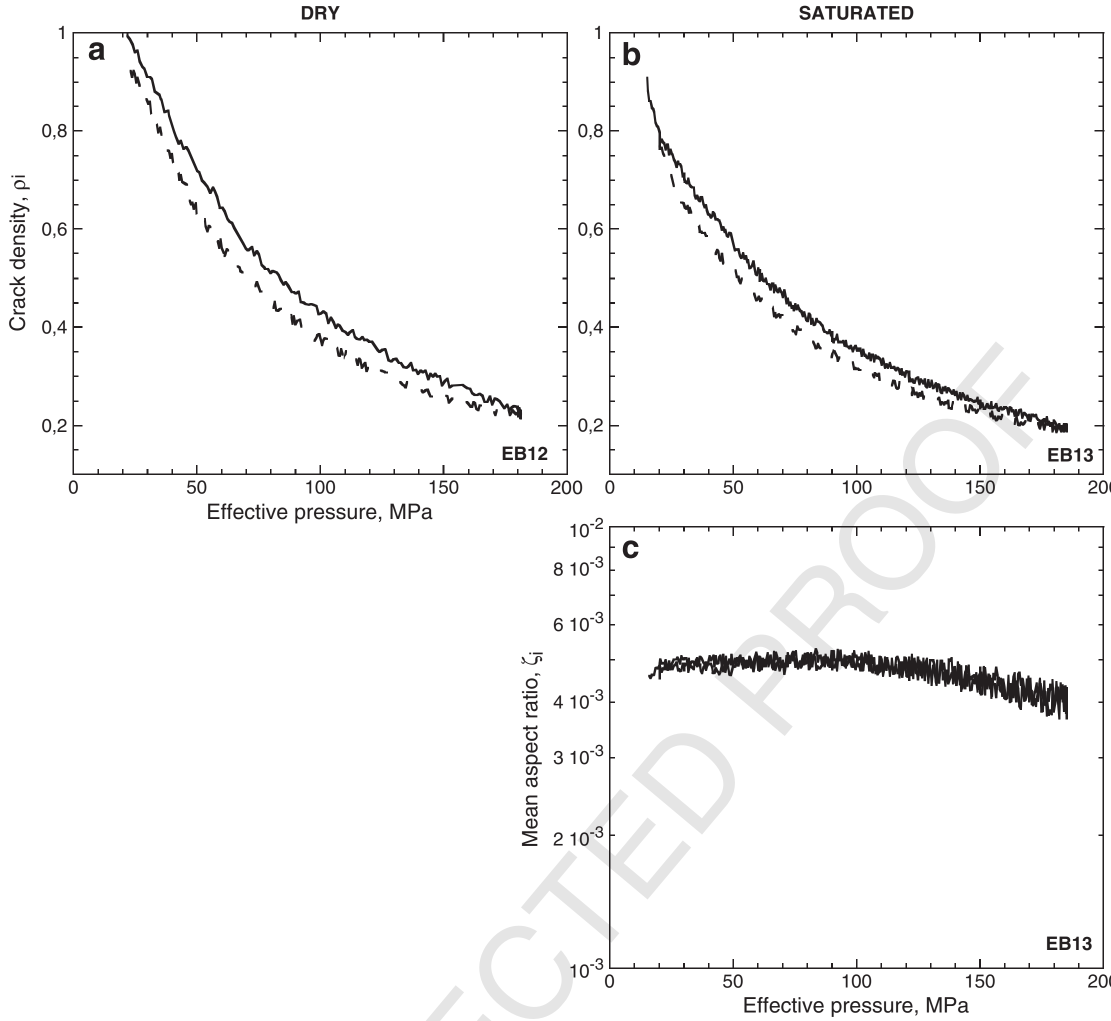

Fig. 3. Evolution of crack density as a function of the effective pressure found in the dry specimen (a) and in the saturated specimen (b). The evolution of the crack density found in the dry case is very similar to the evolution observed in the wet case. (c) Evolution of the mean crack aspect ratio ζ_i as function of the effective pressure. During loading and unloading ζ_i stays almost constant and ~510^{-3}. Unloading is shown as dashed lines.

the *S*-wave velocities. For the dry experiment, *F* is minimized with respect to two variables: ρ_i and ρ_v, whereas, for the wet experiment, *F* is minimized with respect to four variables: ρ_i, ζ_i, ρ_v and ζ_v.

4. Hydrostatic loading

4.1. Mechanical and velocities data – crack density evolutions

Fig. 2a and b summarizes the mechanical data. In dry and in saturated conditions, the samples show similar trend: compaction, in both experiments, at 190 MPa effective confining pressure is ~1%, and the samples show an almost perfectly elastic behavior. Fig. 2c and d illustrates the evolutions of *P*- and *S*-wave velocities with effective confining pressure. As *P*-velocities are the same in different directions during the hydrostatic loading, only Vp_{radial} is plotted. Also, only Vs_{vert} is plotted on Fig. 2 as Vs_{vert} coincides with Vs_{hor}.

During the loading, the elastic waves velocities increased: respectively, by 75% (from 3.1 to 5.5 km/s) and 36% for *P*-waves and *S*-waves in the dry case, and and by 22% (from 5 to 6.1 km/s) and 23% for *P*-waves and *S*-waves in saturated conditions. Similar values were reported by Stanchits et al. (2006) in the dry case, for confining pressure in the range of 10 − 120 MPa, and by Benson et al. (2006) in the saturated case, for confining pressure in the range of 10 − 90 MPa.

Using the effective medium model presented in the previous section we inverted the laboratory-measured elastic wave velocities in terms of crack density and aspect ratio (for the saturated case) at each stepwise increase in pressure. For the inversion, we used, in both dry and wet cases, matrix (crack free) elastic moduli $E_o = 85$ GPa and $\nu_o = 0.3$. These values are found from the axial loading assuming that during the loading and before the rupture the extra compliances ΔS_{ii} cannot be negative. Note that the value of E_o and ν_o used here are closed to those found in the study of Stanchits et al. (2006). In the saturated case, the fluid bulk modulus was taken as $K_f = 2$ GPa. The evolution of the crack density due to increasing effective pressure is shown in Fig. 3a) for the dry case and in Fig. 3b) for the saturated case. Note the vertical cracks ρ_v is equal to 0 in these inversions, as no anisotropy in the velocities is observed, then only the evolution of the randomly oriented cracks density ρ_i is plotted. As effective pressure increase from 10 MPa to 190 MPa crack density decreases from approximately 1 to approximately 0.2. It is interesting to note that the evolution of crack density is almost the same in the dry and saturated cases, although the measured elastic wave velocities are different in these two cases (Fig. 2).

In the saturated experiment, and over the same pressure range, the crack aspect ratio stays almost constant and $\zeta_i \simeq 510^{-3}$ (Fig. 3c). For this experiment, the crack porosity can be estimated using the simple relation $\Phi = \pi \rho_i \zeta_i$. This relation assumes that all the porosity within the sample is composed of penny shaped cracks. However, as noticed by several authors (Benson et al., 2006; Adelinet et al., 2010), basalt sample may possess a quasiequant porosity which could be due to the formation of gas bubbles within the lava flow. Such porosity is almost insensitive to the pressures used in this study, and as a consequence has almost no impact on the evolution of the velocities with pressure. Thus, the evolution of the porosity in Etna basalt may be estimated using the following relation:

$$\Phi = \pi\rho_i\zeta_i + \Phi_o, \tag{21}$$

where Φ_o is the equant porosity. Fig. 4 compares the evolution of the porosity inferred directly from strain gages measurements assuming an initial porosity of 4.7%, with the porosity inferred from Eq. (21). A good agreement between the model and the experimental data is found for a value of the equant porosity fixed to $\Phi_o = 3.45\%$. This value of the equant porosity is consistent with the study of Adelinet et al. (2010).

4.2. Permeability evolution

The permeability evolution during increase of the effective pressure is given on Fig. 5. As the effective pressure increases from 10 MPa to 190 MPa the permeability decreases by more than two orders of magnitude: from 10010^{-18} m^2 to0.910^{-18} m^2. This behavior highlights the elastic crack closure and is entirely consistent with the behavior of the mechanical data (Fig. 2b) and the crack density evolution (Fig. 3b). It is also interesting to observe that the measurements made from 1) the steady state flow at fixed pressure, 2) the pulse procedure also done at fixed pressure, and 3) the measurements done during increasing loading (continuous record) are in very good agreement. During the unloading, a small hysteresis appears: at 20 MPa effective pressure, the permeability after loading is 1510^{-18} m^2, whereas is was 3010^{-18} m^2 before loading. This change in permeability is very small, which tends to prove that the behavior of the basalt is almost elastic in the range of $10-190$ MPa.

In the case of a highly micro-fractured rock, Guéguen and Dienes (1989) showed that permeability can be represented as that of a rock containing penny shaped cracks. In such cases, the permeability k can be expressed as:

$$k = \frac{2}{15} f w_i^2 \zeta_i \rho_i, \tag{22}$$

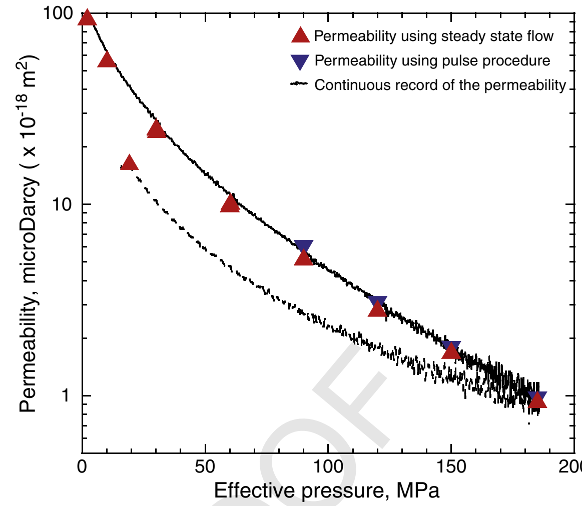

Fig. 5. Permeability evolution for the hydrostatic loading on sample EB13. Permeability measurements were made using three techniques; 1) using steady state flow (Darcy low) (symbol ▲), 2) using pulse procedure (symbol ▼) and 3) by applying a constant pore fluid pressure gradient during the loading (see Section 2.2 for details). The agreement between the data obtained by these three techniques is good. During loading, the permeability decrease of more than 2 orders of magnitude, due to the closure of the pre-existing cracks. Unloading is shown as dashed line.

where w_i is the crack average aperture and f is the connectivity factor. Using the results of the wave velocity inversions (crack density ρ_i, and aspect ratio ζ_i as a function of pressure), and assuming that connectivity factor $f = 1$, it is possible to predict from Eq. (22), the evolution of the mean aperture w_i as a function of pressure. The result is given in Fig. 6.

Pre-existing cracks in the undeformed specimens are due to thermal cracking during formation of basalt; thus the mean crack length of these cracks should be closed to the mean grain size. The initial mean crack aperture at 10 MPa effective pressure is ~0.3 μm. Recalling that the aspect ratio ζ_i is defined as $\zeta_i = w_i/c_i$, this leads to a initial mean crack radius $c_i \simeq 0.6$ mm (using mean aspect ratio $\zeta_i = 510^{-3}$), or a mean crack diameter of 1.2 mm. This value is consistent with the grain size, which ranges from 0.9 mm to 1.8 mm

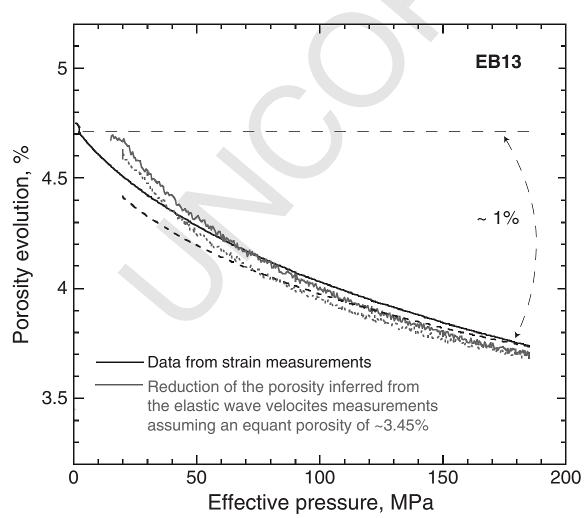

Fig. 4. Comparison between the evolution of the porosity inferred from strain gages measurements assuming an initial porosity of 4.7% (black curve) with the porosity inferred from the effective medium model assuming that the porosity evolution is $\Phi = \pi\rho_i\zeta_i + \Phi_o$, where Φ_o is the equant porosity estimated to 3.45% (grey curve). Unloading is shown as dashed lines.

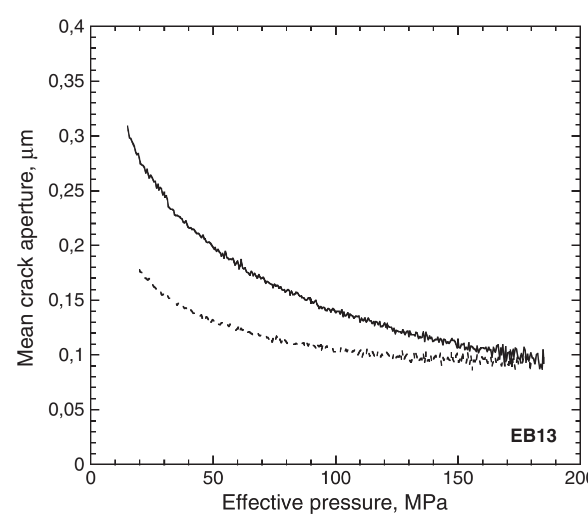

Fig. 6. Evolution of mean crack aperture w as a function of the effective pressure in the saturated specimen. The mean crack aperture w is deduced from a combination of i) the permeability data and ii) the crack density ρ_i and mean crack aspect ratio ζ_i obtained by the effective medium model (Fig. 3b and c). The mean crack aperture decreases slightly from 0.3 μm to 0.1 μm. Unloading is shown as dashed line.

Please cite this article as: Fortin, J., et al., Influence of thermal and mechanical cracks on permeability and elastic wave velocities in a basalt from Mt. Etna volcano subjected to elevated pressure, Tectonophysics (2010), doi:10.1016/j.tecto.2010.09.028

(Stanchits et al., 2006). Fig. 6 shows also that the mean crack aperture decreases exponentially with increasing effective pressure, in agreement with the empirically law used in simulation of fractured porous media (Taron et al., 2009). However, the decrease in aperture with pressure remains slight as the mean aperture decreases from ~0.3 μm to ~0.1 μm at 190 MPa effective pressure and can justify the hypothesis done in the study of Benson et al. (2006), where the mean aperture is supposed to be constant. The crack density and aspect ratio evolutions show a perfect elastic behavior with effective pressure (Fig. 3b and c), however, permeability evolution shows a small hysteresis with loading–unloading; as a consequence from Eq. (22) a small hysteresis is observed in the evolution of the mean crack aperture with loading–unloading. This observation shows that the mechanical component of fracture closure may not a completely reversible process, but can exhibits small hysteresis as governed by both the elastic and plastic properties of the contacting asperities.

5. Axial compression loading

5.1. Mechanical, velocities, permeability data and AEs localization

In the second part of the loading, the basalt specimens, in the dry and saturated cases, were subjected to axial compression loading at a fixed effective confining pressures of 20 MPa. With increasing axial stress, basalt samples show in both cases, initial overall elastic compaction, and then compaction reverses to dilatancy at a stress state D' labeled on Fig. 7 (Heap et al., 2009a). This behavior suggests the initiation and propagation of dilatant cracks, and is typical of the brittle regime faulting (Paterson and Wong, 2005). Fig. 7b, shows also, that the volumetric strain, in the saturated cases, obtained from strain gages and from pore volume variation are in good agreement, which confirms that the methodology presented in the Section 2 to estimate the pore volume change is satisfactory.

Both specimens were loaded up to failure, which occurs at a maximum deviatoric stress closed to 420 MPa and a maximum axial strain $\varepsilon_1 \simeq 1.1\%$ (Fig. 8a and b). During the axial loading, *P*- and *S*-wave velocities in dry and saturated specimens show significant anisotropy (Fig. 8c and d). Vp_{axial} velocities are higher than Vp_{radial}, and S-waves show acoustic birefringence with Vs_{vert} always being faster than Vs_{hor} in agreement with previous studies (Bonner, 1975; Lockner et al., 1977; Aylin et al., 1995; Stanchits et al., 2006). *P*-wave anisotropy and *S*-wave birefringence increase with increasing axial stress, in addition, Vp_{radial} as well as the *S*-wave decrease with increasing axial loading. These observations suggest the initiation and propagation of cracks, in agreement with the porosity evolution (Fig. 7); they also suggest that the stress-induced cracks are mainly vertically oriented with crack plane normal directions defining a zone perpendicular to the axial stress direction.

The permeability evolution during increase of the deviatoric stress is given on Fig. 9. As the deviatoric stress increases from 0 MPa to 250 MPa the permeability decreases from $1710^{-18}m^2$ to $710^{-18}m^2$. Then with increasing deviatoric stress from 250 MPa up to failure the permeability evolution reverses and increases from 710^{-18} m^2 to 1310^{-18} m^2. The behavior of the permeability is consistent with porosity evolution (Fig. 7b), where first elastic compaction is observed and then dilatancy occurs. However, the change in permeability is relatively small during the deviatoric loading in comparison with our measurements done during hydrostatic loading, where a change in permeability of more than two orders of magnitudes was observed (Fig. 5). We also measured the permeability just after rupture (▲ measurement after rupture on Fig. 9): the permeability of the sample after rupture is $\sim 2810^{-18}$ m^2, indicating that the fracture may act as a drain, in agreement with the study of Nara et al. (2010).

Fig. 10 shows the total Acoustic Emissions distribution for the dry and saturated experiments (Fig. 10 Top, and Bottom respectively). In both experiments, AE localizations are at first rather homogeneously distributed in the sample (stage a); and start localizing when close to failure (stages c and d). Looking at the AE temporal distributions, one can notice that most of the event we were able to localize occur at the very pre-peak and post-peak stage, in agreement with studies done on granite (e.g Lockner et al., 1991; Schubnel et al., 2003). In Fig. 10, the AE localizations (stages b and c, with strain stages defined in Fig. 8a and b) due to the nucleation and propagation of the fault plane can also be compared to the picture of sample after loading. Indeed Fig. 10d (top and bottom) shows pictures of the samples after loading (the samples were impregnated with blue epoxy and cut in half perpendicular to the fault); and we can see that AE localizations and the microstructure of fractured samples are in very good correspondence.

AE localizations give us an image of the pre- and post-failure localization, but provides sparse information on the actual crack distribution in the rock before those stages. In addition, from AE

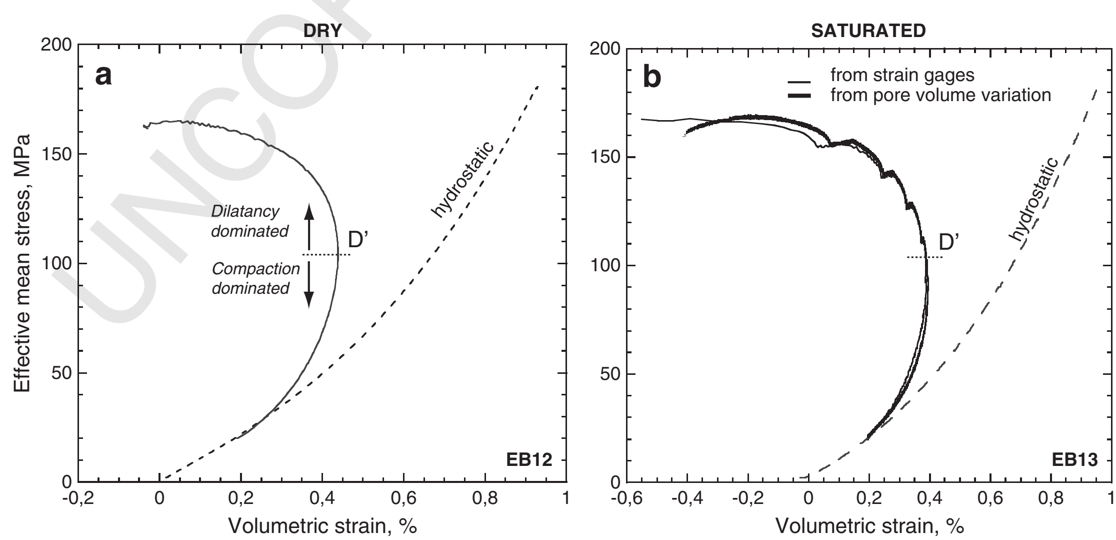

Fig. 7. Effective mean stress versus volumetric strain for the triaxial compression experiments done on sample EB12 in dry condition (a) and on sample EB13 in saturated condition (b). The specimens switch from compaction-dominated behaviour to dilatancy-dominated behaviour at a stress state D' (Heap et al., 2009a). In both experiments the effective confining pressure is fixed to 20 MPa. For the experiment done in the wet condition, the volumetric strain is obtained by two different techniques 1) strain gages (grey curve in Figure (b)) and pore volume variation (black curve in Figure (b)) (2). For reference, hydrostatic loading is shown as dashed lines.

Please cite this article as: Fortin, J., et al., Influence of thermal and mechanical cracks on permeability and elastic wave velocities in a basalt from Mt. Etna volcano subjected to elevated pressure, Tectonophysics (2010), doi:10.1016/j.tecto.2010.09.028

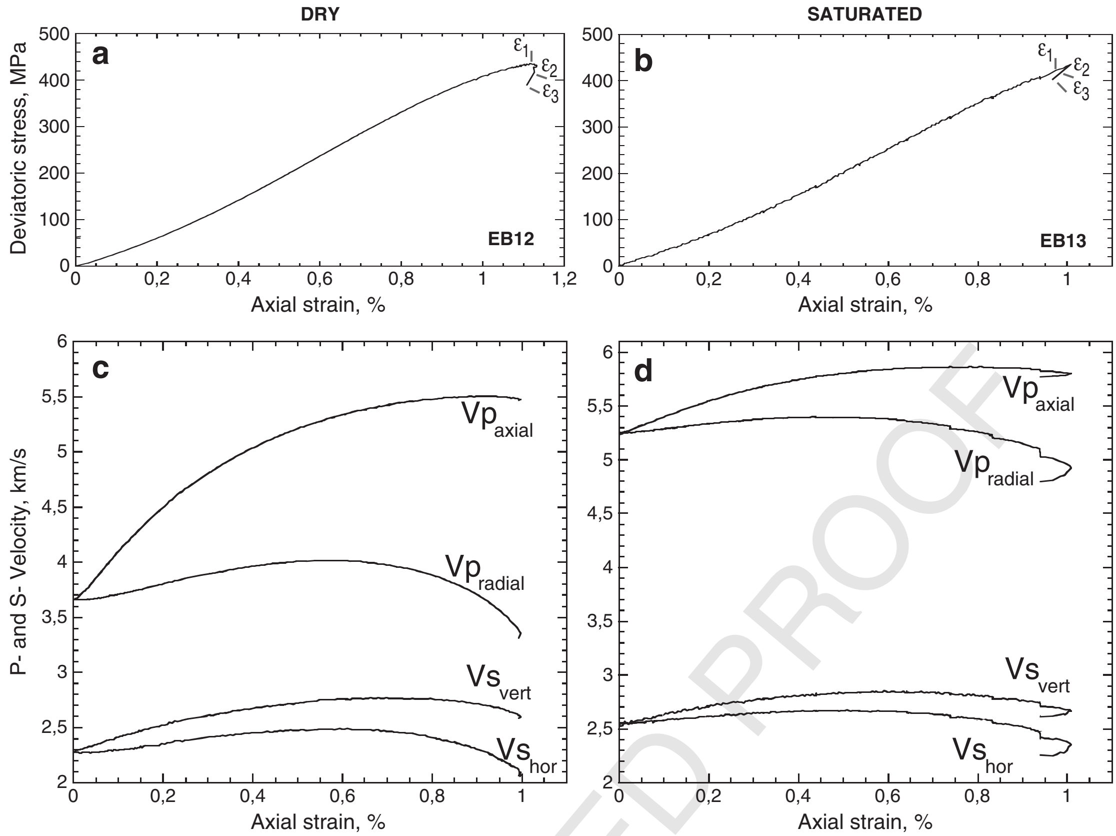

Fig. 8. Mechanical data and velocity measurements for the triaxial compression experiment on EB12 done in dry condition and on EB13 done in saturated condition. (a) and (b) deviatoric stress versus axial strain. (c) and (d) *P* and *S* wave velocities versus axial strain.

localization, we can assume that the effective medium model can be used till the very end of the loading, just before the localization which occurs at stages b and c.

5.2. Microstructural observations

Tested and intact samples were vacuum impregnated with a blue, low-viscosity resin and cut in order to obtain thin sections. Two thin sections were prepared from intact sample (EB9), and three from the sample loaded up to failure in dry condition (EB12). For the intact sample, three randomly located areas were investigated. For the failed sample (EB12), eight areas where selected (zones *A1*, *A2*, *A3*, *B1*, *B2*, *B3*, *C1* and *C2* on Fig. 11a and Table 1). Except for *B1* and *B3*, the areas were chosen in proximity of main fractures in order to analyze the spatial evolution of the crack density and anisotropy in the damage zone. SEM images have been then taken of the selected areas.

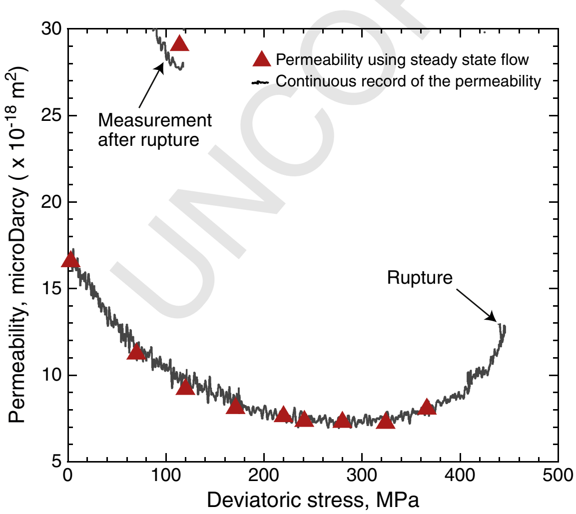

Fig. 9. Permeability evolution during the triaxial loading on sample EB13. Permeability measurements were made: 1) using steady state flow (Darcy low) (symbol ▲), and 2) by applying a constant pore fluid pressure gradient during the loading. During the triaxial loading, the permeability first decreases from 17.10^{-18}m^2 to 7.10^{-18}m^2 and then increases 7.10^{-18}m^2 to 12.10^{-18}m^2 as vertical cracks initiate and propagate.

Stereological measurements were performed for undeformed, and failed samples (Fig. 11a and Table 1). We counted the number of crack intersections with an overlapping grid (Underwood, 1970). Spacing between two consecutive lines of the grid has been fixed at 10 µm (Fig. 11b) and only cracks with width higher than 0.3 µm have been taken into account. The grid has been applied both along and perpendicularly with respect to the loading, we denote the line a intercept density (number of crack intersections per unit length) for the array oriented parallel to σ_1 by $(P_L)_\parallel$, and that for the perpendicular array by $(P_L)_\perp$; the anisotropy Ω_{12} is measured as (Wu et al., 2000):

$$\Omega_{12} = \frac{(P_L)_\perp - (P_L)_\parallel}{(P_L)_\perp + (4/\pi - 1)(P_L)_\parallel}. \quad (23)$$

Crack densities, $(P_L)_\parallel$ and $(P_L)_\perp$ are summarized in Table 1. From this study we measure crack density in the range of values found in other experimental studies (Wong, 1982; Wu et al., 2000; Janssen et al., 2001) and we found that no clear changes between $(P_L)_\parallel$ and $(P_L)_\perp$ of failed samples with respect to the ones calculated for undeformed samples were observed (Table 1). However when crack anisotropy is taken in account, systematically higher values (about 2–3 times) were found (Table 1, Fig. 11c), indicating that cracks along the loading direction formed and/or propagated. This pattern is also

Please cite this article as: Fortin, J., et al., Influence of thermal and mechanical cracks on permeability and elastic wave velocities in a basalt from Mt. Etna volcano subjected to elevated pressure, Tectonophysics (2010), doi:10.1016/j.tecto.2010.09.028

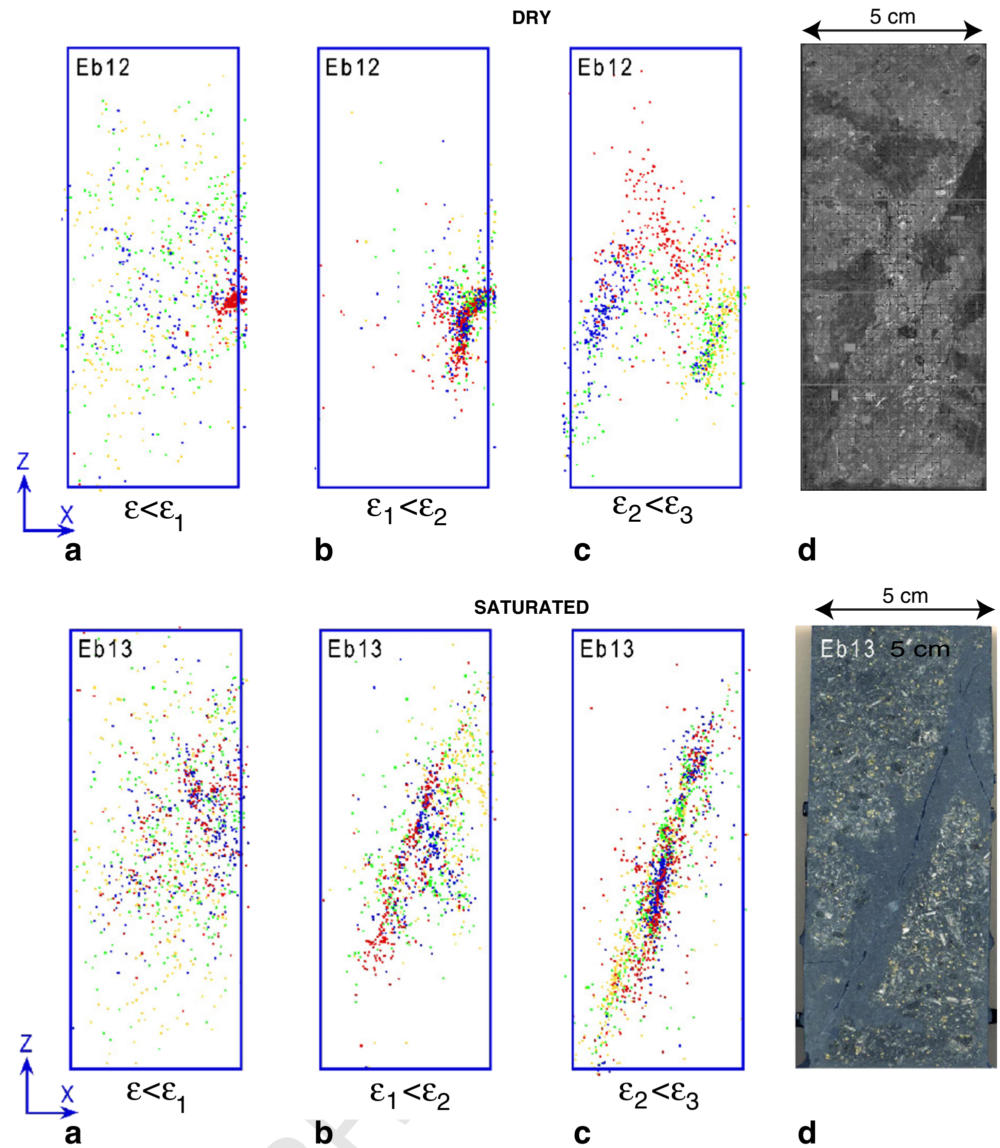

Fig. 10. a) a) AE hypocenter distribution for sample deformed in dry condition (top plot), and in saturated condition (bottom plot). Color code of dots indicates time sequence of AE events for each snap-shot starting with yellow through green, blue and finally, red hypocenters. The strain interval are defined in Fig. 8a and b. Fig. 10d (top and bottom plots) are pictures of the samples after loading. The samples were impregnated with blue epoxy and cut in two. (For interpretation of the references to color in this figure legend, the reader is referred to the web version of this article.)

evident from the crack distribution analysis relative to the cracks in proximity (~1*mm*) of the main fractures. The crack surface area per unit volume, *SV*, can be calculated as (Wu et al., 2000):

$$SV = \frac{\pi}{2}(P_L)_\perp + \left(2 - \frac{\pi}{2}\right)(P_L)_\parallel. \tag{24}$$

The evolution of the crack surface area, *SV* is given as a function of the distance from fracture on Fig. 11d. A rapid decrease of *SV* towards the background values can be observed at a distance of about 1.5 mm. Taken together the microstructural analysis is consistent with the mechanical data, as well as the velocity data which show that deformation was mainly cracks driven and related to opening and shearing of pre-existing cracks.

Finally a Field Emission Gun-Scanning Electron Microscope (FESEM) installed at *Instituto Nazionale di Geofisica e Vulcanologia*, Rome (Italy) has been used to map at high resolution larger areas (tens of mm), by linking hundreds of images. A magnification of 80× has been selected and the analysis has been carried out on the sample EB13 led to failure (Fig. 12). One can observe the shear localization, but also long microcracks, propagating thorough both the glassy matrix and crystals. The damage zone near the localization is narrows, and tends to confirm that strain localisation is mainly driven from pre-existing cracks, due to thermal origin (Vinciguerra et al., 2005).

5.3. Crack density evolution inverted from elastic wave measurements

Using the effective medium model presented in Section 3, the velocities can be inverted in terms of two crack densities: the first one ρ_i which characterizes cracks randomly oriented, this population is associated with the pre-existing cracks; and a second crack density, ρ_v, which characterizes vertical cracks, which approximates the crack distribution resulting from axial loading. The results of the inversion of the measured elastic wave velocities are shown in Fig. 13c and d, for the sample deformed in the dry and saturated cases respectively. In this inversion we used the same matrix (crack free) elastic moduli E_o and ν_o as in the previous section.

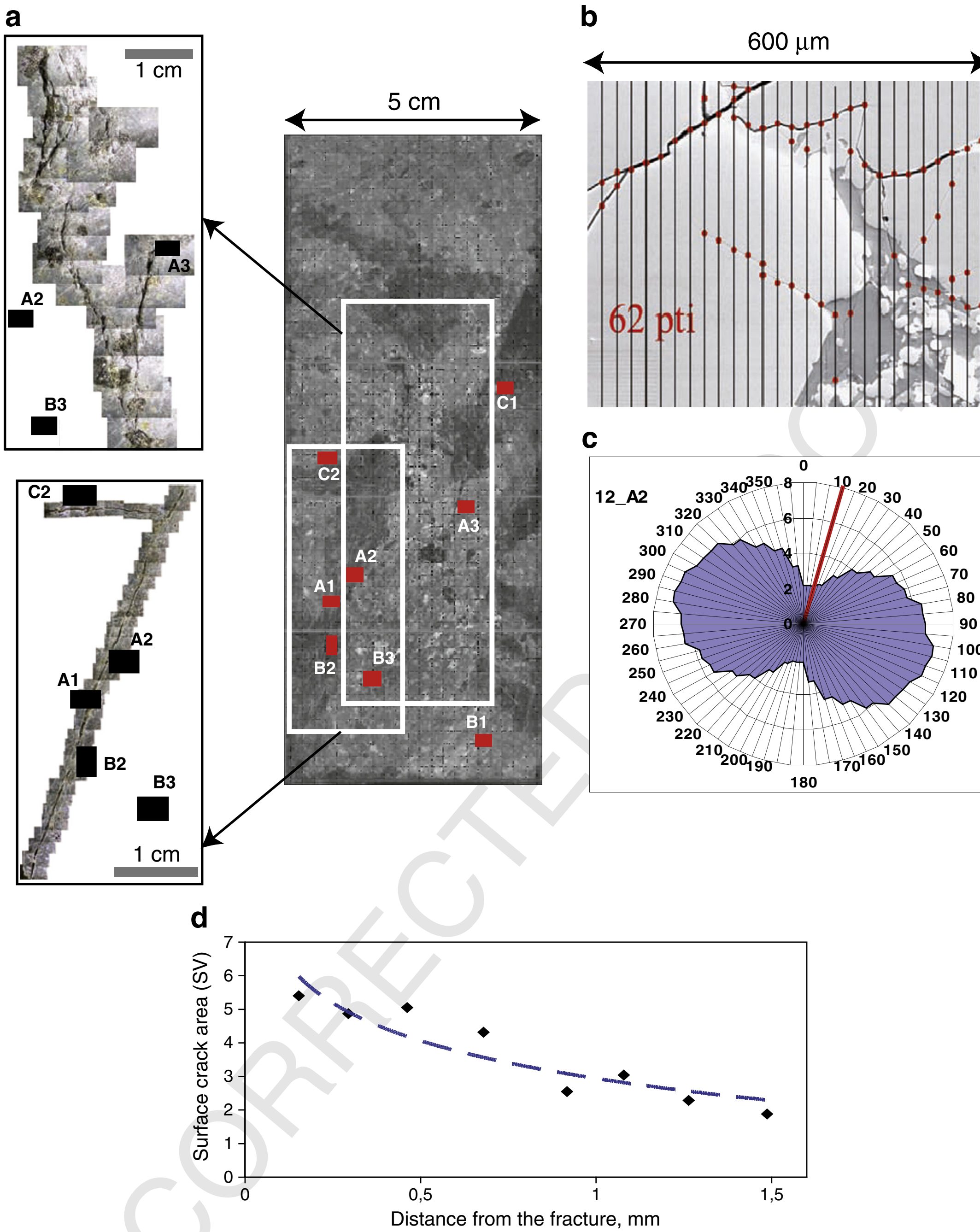

Fig. 11. a) Optical images of fractures in the failed sample (EB12). Red labels on the central image indicate areas investigated throughout SEM images. b) Example of stereological measurement through grid intersection methods Underwood (1970), where unit is in mm^{-1}. c) Crack anisotropy distribution through Underwood method. Red line indicate load direction. d) Evolution of the surface crack area as a function of the distance from the main fracture. (For interpretation of the references to color in this figure legend, the reader is referred to the web version of this article.)

In the dry case (Fig. 13c), ρ_i is closed to 0.9 at the beginning of the axial loading, whereas $\rho_v = 0$, in agreement with the results obtained during the hydrostatic loading (Fig. 3a). With increasing axial loading the density of randomly oriented cracks decreases from 1 to 0, whereas the vertical crack density increases from 0 to 1 just before the failure. Fig. 13a plots also the forward solution of the crack densities to yield a calculated *P*- and *S*-elastic wave velocity (symbols ○) for comparison with the laboratory data used as input for the inversions (solid lines). The agreement between the data and the forward solution via the effective medium model is very good, and indicates that an effective medium model considering two different populations of cracks is appropriated to describe the evolution of the velocities during axial loading in basalt sample.

Fig. 13d and e shows the inversion of the velocities for the saturated case. The evolution of crack densities (Fig. 13d) is similar to the observation made in the dry case (Fig. 13c): with increasing axial load, the randomly oriented crack density decreases, whereas the vertical crack density increases. In the saturated case, it is also possible to estimate the mean crack aspect ratio of the two considered populations of cracks (ζ_i and ζ_v). The mean aspect ratio of the randomly oriented cracks (Fig. 13e) is similar to the value obtained during the hydrostatic loading $\zeta_i \simeq 510^{-3}$ and decreases slightly with increasing axial strain. The mean aspect ratio of the vertical cracks is almost constant during the loading and $\zeta_v \simeq 10^{-2}$. The effective medium model used to do this inversion does this assumption that the two populations of cracks are independent, however Fig. 13c and d

Table 1
Linea intercept density $(P_L)_\perp$, $(P_L)_\parallel$, and crack distribution anisotropy (Eq. (23)) measured for undeformed (EB9) and failed (EB12) samples. The starting position is arbitrary for the undeformed material, while it corresponds to the load direction for the failed samples EB12.

Thin section	Number of images	$(P_L)_\perp$,	$(P_L)_\parallel$	Anisotropy %
EB9-1	8	0.96*	1.15*	12
EB9-2	20	1.38*	0.91*	−28
EB9-3	25	1.41*	1.60*	8
EB12-A1	28	1.26	2.51	39
EB12-A2	20	1.37	2.07	24
EB12-A3	21	0.69	1.53	44
EB12-B1	16	0.11	0.20	34
EB12-B2	44	1.55	4.20	52
EB12-B3	25	0.42	0.81	37
EB12-C1	24	1.51	2.69	33
EB12-C2	16	0.71	1.82	50

can also be interpreted as followed: during axial loading, at the beginning of the loading, cracks with normals within planes parallel to the maximum compressive stress direction (Ox_3) became closed with increasing load, which results in a apparent decrease of the randomly oriented crack density and an increase if the vertical crack density. In this second interpretation, the crack aspect ratio of the two populations of cracks should be equal and in fact, we can see from Fig. 13e, that ζ_i and ζ_v are close. This result tends to show, that our model, which considers 4 microstructural parameters ρ_i, ρ_v, ζ_i and ζ_v might be simplified using $\zeta_i = \zeta_v$.

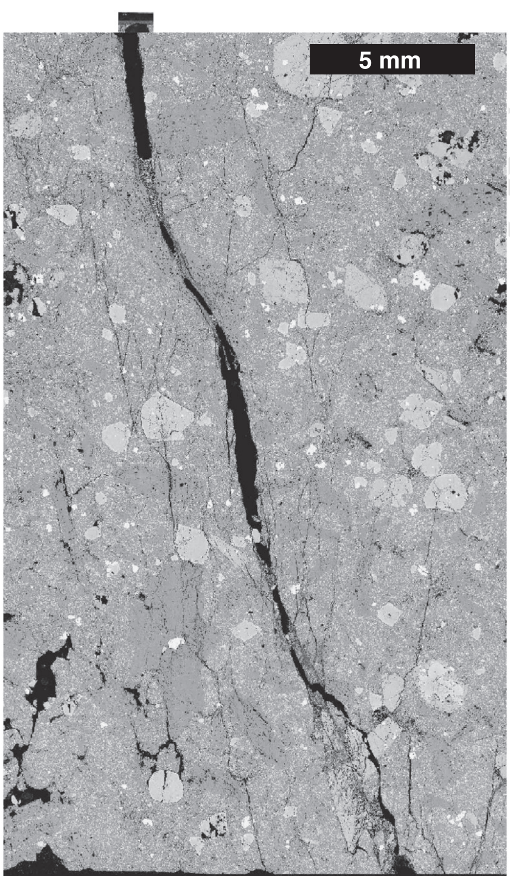

Fig. 12. FESEM higher resolution map of fractures forming at failure in EB13 (saturated sample). For this sample, the maximum compressive stress direction was vertical.

The evolution of the porosity in Etna basalt, during the axial loading, may be estimated using the following relation:

$$\Phi = \pi\rho_v\zeta_v + \pi\rho_i\zeta_i + \Phi_o, \tag{25}$$

where Φ_o is the equant porosity fixed to 3.45%. Fig. 14a compares the evolution of the porosity inferred directly from strain gages measurements with the porosity inferred from Eq. (25). Keeping in mind that the relation which describe the porosity is very simple, Fig. 14a shows that the model porosity trend is good; the model shows first compaction and then dilatancy. With increasing load, a small discrepancy appears between the model and the experimental data, but the difference remains small (less than 0.5%).

Different theoretical model can be used to predict the evolution of permeability due to stress-induced microcracking. For example Zhu and Wong (1999) simulated dilatancy and the resulting permeability evolution implicity by incorporating an increasing number of cracks into a random network model. Simpson et al. (2003) combined crack parameters and their evolution as a function of stress, explicitly on the basis of fracture mechanics with a statistical permeability model (Dienes, 1982). Here we used a simple model based also on statistical permeability model (Guéguen and Dienes, 1989): from our effective medium model we are able to distinguish two populations of cracks, then we can assume that the randomly oriented cracks are characterized by a permeability k_i, and the vertical cracks by a permeability k_v. Then, the global permeability k of the sample can be modeled using the Voigt average:

$$k = k_i + k_v. \tag{26}$$

k_i and k_v can be calculated from the model of Guéguen and Dienes (1989), and:

$$k = \frac{2}{15} f\left(w_i^2 \zeta_i \rho_i + w_v^2 \zeta_v \rho_v\right). \tag{27}$$

The above equation is valid if the distribution functions for the various crack parameter are narrow. We follow this assumption, and also assume that the connectivity factor $f = 1$. The cracks parameters $\zeta_i, \rho_i, \zeta_v, \rho_v$ are deduced from the inversion of the elastic wave velocities (Fig. 13c and d). We assume that the mean crack averages w_i and w_v are constant. The mean crack aperture of the randomly oriented crack, w_i can be deduced from the Fig. 6 and is fixed to 0.18 μm. Then the only unknown crack parameter is the mean crack aperture of the vertical cracks, w_v. Fig. 14b shows the evolution of the permeability estimated from (27), assuming $w_v = 0.12$ μm (curve 1 on Fig. 14b); and assuming $w_v = 0.1$ μm (curve 3 on Fig. 14b); the experimental permeability data are given by the curve 2. From Fig. 14b, we see that the permeability model reproduces well the experimental data, demonstrating at first a decrease and then an increase of the permeability. Fig. 1 3b, shows also, that the estimation of the mean crack average of the vertical cracks is constrained, indeed $0.12 > w_v > 0.1$ μm, a value which is close to mean crack average of the randomly oriented cracks, $w_i = 0.18$ μm.

6. Conclusion

We investigated in this study the evolution of compressional and shear-wave velocities, permeability, porosity and acoustic emission of Etna basalt in hydrostatic and triaxial compression tests done at 20 MPa effective confining pressure. The experiments were done in dry and saturated conditions.

With increasing hydrostatic pressure up to 190 MPa, *P*- and *S*-wave velocities in basalt increase which is interpreted by the closure of pre-existing cracks. Using a micromechanical model based on effective medium concepts, the velocity measurements were inverted in term of crack density evolution. In this case, the cracks are assumed to be

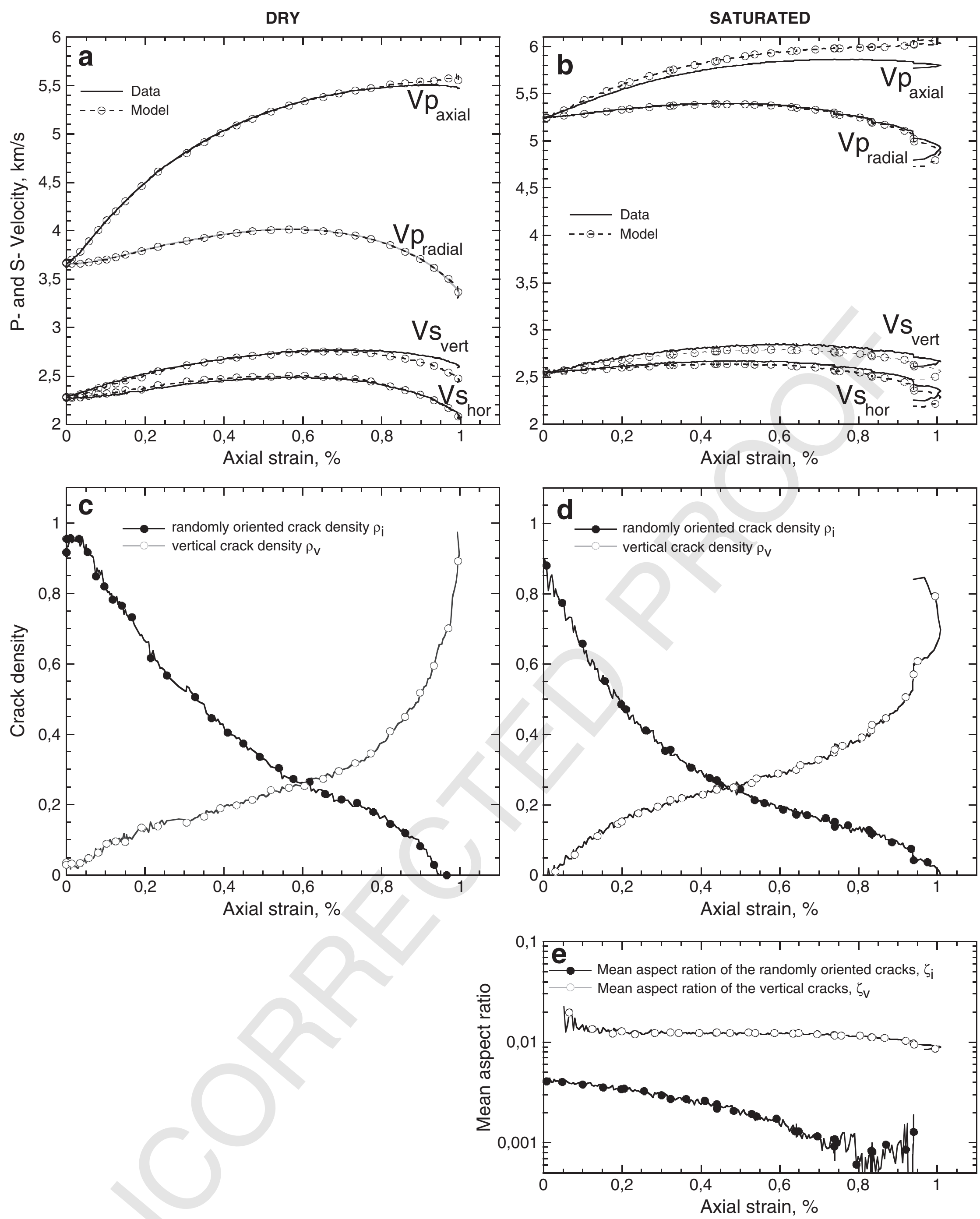

Fig. 13. Evolution of velocities and crack density as a function of axial strain. (a) and (b) *P* and *S* wave velocities versus axial strain (data is indicated by a line and the forward solution derived from the effective medium model is indicated by symbols ○.) (c) and (d) Evolution of the randomly oriented crack density (symbol ●) and the vertical crack density (symbol ○) as a function of axial strain. (e) Evolution of the mean crack aspect ratio of i) the randomly oriented cracks ζ_i (symbol ●) and ii) of the vertical cracks ζ_v (symbol ○).

randomly oriented. Our prediction shows that as effective pressure increases from 10 to 190 MPa, the crack density decreases from *im*1 to 0.2, and the trend is similar both in the dry and saturated loading. The effect of pre-existing cracks closure is also highlight by permeability evolution which decreases from 10010^{-18} m^2 to 0.910^{-18} m^2 as effective pressure increases. Using the statistical permeability model of Guéguen and Dienes (1989), we are able to inferred from the elastic wave velocity and permeability data the evolution of the mean crack aperture with increasing loading: the mean crack aperture is found to decrease slightly from ~0.3 µm to ~0.1 µm as effective pressure increases from 10 to 190 MPa.

In triaxial compression experiments performed at 20 MPa effective confining pressure P-wave anisotropies and shear-wave birefringence develop in both dry and wet conditions. In this case we use a micromechanical model which considers two populations of cracks. Thus, the velocity measurements are inverted in term of two crack densities: ; ρ_i, the pre-exiting crack density where the cracks are supposed to be randomly distributed and ρ_v, the vertical crack density, which characterized the cracks induced by the deviatoric loading. Our prediction shows that as deviatoric stress increases from 0 to 250 MPa, ρ_i decreases from ~0.9 to 0, whereas ρ_v increases from ~0 to 1, and like is the hydrostatic loading the trend during the deviatoric loading is similar both

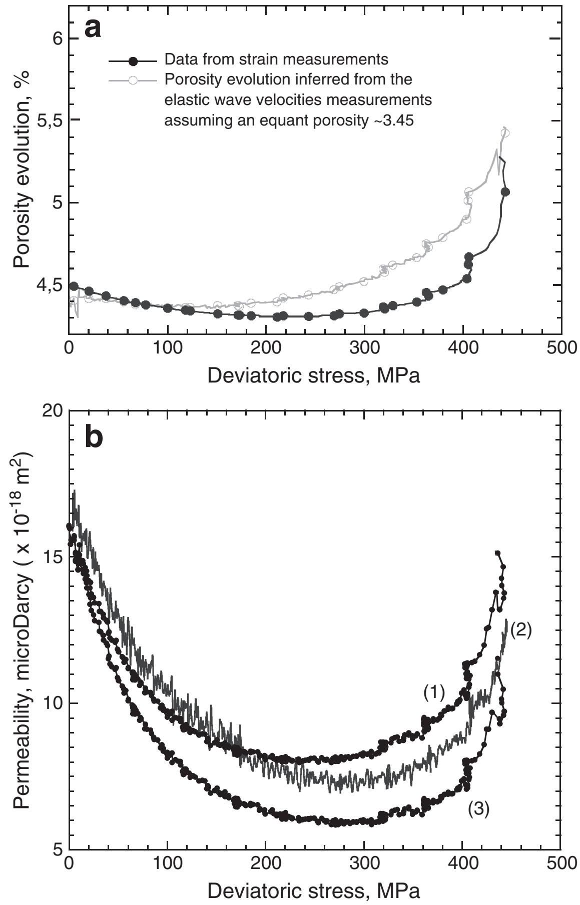

Fig. 14. a) Comparison between the evolution of the porosity inferred from strain gages measurements assuming an initial porosity of 4.7% (black curve) with the porosity inferred from the effective medium model assuming that the porosity evolution is $\Phi = \pi\rho_i\zeta_i + \pi\rho_v\zeta_v + \Phi_o$, where Φ_o is the equant porosity estimated to 3.45% (grey curve) b) The permeability can be modeled using the Voigt average of i) the permeability of a medium containing randomly oriented cracks (k_i), and 2) the permeability of a medium containing vertical cracks (k_v). k_i and k_v are deduced from the statistical model of Guéguen and Dienes (1989), using respectively the crack parameters ρ_i, ρ_v, ζ_i and ζ_v). The mean crack aperture of the randomly oriented crack is fixed to 0.18 µm. Curve (2) denotes the data, curve (1) and (3) denotes the result inferred from the permeability model with a mean crack aperture of the vertical cracks of 0.12 µm and 0.1 µm, respectively.

in the dry and saturated specimens. The microstructural observations done in deformed samples are consistent with the velocity behavior and show that vertical crack propagate. The competition between pre-existing cracks closure and nucleation and propagation of newly-formed vertical cracks could also be seen from the permeability evolution, which decreases in the first part of the deviatoric loading from 1710^{-18} m^2 to 710^{-18} m^2 and then increases with the propagation of vertical cracks from 710^{-18} m^2 to 1310^{-18} m^2. Finally, the permeability evolution can be predicted from elastic wave velocity measurements, with assumptions made of the mean crack aperture.

The observed relations between damage state, elastic properties and microseismic source types can also be used to improve our understanding of the pre-eruptive seismic patterns observed at Mt. Etna volcano. The experimental observations of low AE activity and propagation of shear cracks through previously formed tensile cracks are in good agreement with the prevalence of strike-slip mechanisms inferred from focal solutions of earthquakes preceding volcanic eruptions. The absence of a significant dilatant phase loading can explain the lack of significant ground deformation and the increase of seismicity at a short term (days to hours) before the opening of eruptive fracture systems. Moreover changes in permeability can also be related to the change in fluid saturation observed before major eruptive events (Patanè et al., 2003).

Acknowledgements

We thank Georg Dresen for his support in this project, and Stefan Gehrman (both at GFZ) for preparing the thin sections. Concetta Trovato is thanked for the help in the microstructural observations. Sergio Vinciguerra was supported by the firb-miur (Sviluppo Nuove Tecnologie per la Protezione e Difesa del Territorio dai Rischi Naturali). M. Heap and P. Benson are strongly acknowledged for the accurate revision of the manuscript. P. Baud and A. Schubnel are also acknowledged for the fruitful discussions.

References

Adelinet, M., Fortin, J., Guéguen, Y., Schubnel, A., Geoffroy, L., 2010. Frequency and fluid effects on elastic properties of basalt: experimental investigations. Geophysical Research Letters 37, L02303 doi:10.1029/2009GL041660.
Aylin, M., Meredith, P., Murrel, A., 1995. Microcracking during triaxial deformation of porous rocks monitored by changes in rock physical properties, I. elastic-wave propagation measurements on dry rocks. Tectonophysics 245, 205–221.
Benson, P., Schubnel, A., Vinciguerra, S., Trovato, C., Meredith, P., Young, R., 2006. Modeling the permeability evolution of microcracked rocks from elastic wave velocity inversion at elevated isostatic pressure. Journal of Geophysical Research 111, B04202 doi:10.1029/2005JB003710.
Benson, P., Vinciguerra, S., Meredith, P., Young, R., 2008. Laboratory simulation of volcano seismicity. Science 322 (5899), 249 doi:10.1126/science.1161927.
Bonner, B., 1975. Shear-wave birefringence in dilating granite. Geophysical Research Letters 1, 217–220.
Brace, W., Walsh, J., Frangos, W., 1968. Permeability of granite under high pressure. Journal of Geophysical Research 73, 2225–2236.
Briole, P., Nunnari, G., Puglisi, G., Murray, J., 1990. The 1989 September–October eruption of mt. Etna (italy): some quantitative information obtained by geodesy and tiltmetry. C.R. Acad. Sci. Paris 310 (II), 1747–1754.
Bristow, J., 1960. Microcracks and the static and dynamic constants of annealed and heavily cold-worked metals. Journal of Applied Physics 11, 81–85.
Burlini, L., DiToro, G., 2008. Geophysics: volcanic symphony in the lab. Science 322 (5899), 207 doi:10.1126/science.1164545.
Castellano, M., Ferrucci, F., Godano, C., Imposa, S., Milano, G., 1993. Upwards migration of seismic focii: a forerunner of the 1989 eruption of Mt Etna (Italy). Bull. Volcanol. 55, 357–361.
Dienes, J., 1982. Permeability, percolation and statistical crack mechanics. In: Goodman, R.E., Heuze, F.E. (Eds.), issues in Rock Mechanics, pp. 86–94.
Ferrucci, F., Rasa, R., Gaudiosi, G., Azzaro, R., Imposa, S., 1993. Mt. Etna: a model for the 1989 eruption. J. Volc. Geoth. Res. 56, 35–55.
Fortin, J., Stanchits, S., Dresen, G., Guéguen, Y., 2006. Acoustic emission and velocities associated with the formation of compaction bands in sandstone. Journal of Geophysical Research 111, B10203 doi:10.1029/2005JB003854.
Fortin, J., Stanchits, S., Dresen, G., Guéguen, Y., 2009. Acoustic emissions monitoring during inelastic deformation of porous sandstone: comparison of three modes of deformation. Pure and Applied Geophysics 166, 823–841.
Guéguen, Y., Dienes, J., 1989. Transport properties of rocks from statistics and percolation. Mathematical Geology 21, 1–13.
Guéguen, Y., Kachanov, M., 2010. Effective elastic properties of cracked and porous rocks – an overview. Tectonophysics.
Heap, M., Baud, P., Meredith, P., Bell, A., Main, I., 2009a. Time-dependent brittle creep in darley dale sandstone. Journal of Geophysical Research 114, B07203 doi:10.1029/2008JB006212.
Heap, M., Vinciguerra, S., Meredith, P., 2009b. The evolution of elastic moduli with increasing crack damage during cyclic stressing of a basalt from Mt. Etna volcano. Tectonophysics 471 (1–2), 153–160.
Janssen, C., Wagner, C., Zang, A., Dresen, G., 2001. Fracture process zone in granite: a microstructural analysis. International Journal of Earth Sciences 90, 46–59.
Kachanov, M., 1980. Continuum model of medium with cracks. Journal of Engineering Mechanics Division, ASCE 106 (EM5), 1039–1051.
Kachanov, M., 1994. Elastic solids with many cracks and related problems. In: Hutchinson, J., Wu, T. (Eds.), Advanced in Applied Mechanics, 30. Adacemic Press, pp. 256–426.
LeRavalec, M., Guéguen, Y., 1994. Permeability models for heated saturated igneous rocks. Journal of Geophysical Research 99, 24251–24261.
Lockner, D., Byerlee, J., Kuksenko, V., Ponomarev, A., Sidorin, A., 1991. Quasi-static fault growth and shear fracture energy in granite. Nature 350, 39–42.
Lockner, D., Walsh, J., Byerlee, J., 1977. Changes in seismic velocity and attenuation during deformation of granite. Journal of Geophysical Research 82, 5374–5378.
Mavko, G., Mukerji, T., Dvorkin, J., 1998. The rock physics handbook: tools for seismic analysis in porous media. Cambridge University Press.
Nara, Y., Meredith, P., Yoneda, T., Kaneko, K., 2010. Influence of macro-fractures and micro-fractures on permeability and elastic wave velocities in basalt at elevated pressure. In this issue.

Please cite this article as: Fortin, J., et al., Influence of thermal and mechanical cracks on permeability and elastic wave velocities in a basalt from Mt. Etna volcano subjected to elevated pressure, Tectonophysics (2010), doi:10.1016/j.tecto.2010.09.028

Patanè, D., DeGori, P., Chiarabba, C., Bonaccorso, A., 2003. Magma ascent and the pressurisation of mount Etna's volcanic system. Science 299, 2061–2203.

Paterson, M., Wong, T., 2005. Experimental rock deformation–the brittle field. Springer, Berlin. 347 pp.

Sayers, C., Kachanov, M., 1995. Microcracks induced elastic wave anisotropy of brittle rocks. Journal of Geophysical Research 100, 4149–4156.

Schubnel, A., Benson, P., Thompson, B., Hazzard, J., Young, R., 2006. Quantifying damage, saturation and anisotropy in cracked rocks by inverting elastic wave velocities. Pure and Applied Geophysics 163, 5–6.

Schubnel, A., Guéguen, Y., 2003. Dispersion and anisotropy of elastic waves in cracked rocks. Journal of Geophysical Research 108 (B2) doi:10.1029/2002JB001824.

Schubnel, A., Nishizawa, O., Masuda, K., Lei, X., Xue, Z., Guéguen, Y., 2003. Velocities measurements and crack density determination during wet triaxial experiments on oshima and toki granites. Pure and Applied Geophysics 160, 869–887.

Simpson, G., Guéguen, Y., Schneider, F., 2003. Analytical model for permeability evolution in microcracking rock. Pure and Applied Geophysics 160, 999–1008.

Stanchits, S., Dresen, G., Vinciguerra, S., 2006. Ultrasonic velocities, acoustic emission characteristics and crack damage of basalt and granite. Pure and Applied Geophysics 163 (5–6), 975–994.

Stanchits, S., Fortin, J., Dresen, G., Guéguen, Y., 2009. Initiation and propagation of compaction bands in dry and wet bentheim sandstone. Pure and Applied Geophysics 166, 843–868.

Tanguy, J.-C., Condomines, M., Kieffer, G., 1997. Evolution of the Mount Etna magma: constraints on the present feeding system and eruptive mechanism. J. Volcanol. Geotherm. Res. 75, 221–250.

Taron, J., Elsworth, D., Min, K., 2009. Numerical simulation of thermal–hydrologic–mechanical–chemical processes in deformable, fractured porous media. International Journal of Rock Mechanics and Mining Sciences 46, 842–854.

Underwood, E., 1970. Quantitative stereology. Reading, Addison Wesley, p. 274.

Vinciguerra, S., Trovato, S., Meredith, P., Benson, P., 2005. Relating seismic velocities, thermal cracking and permeability in Mt. Etna and Iceland basalts. International Journal of Rock Mechanics and Mining Sciences 42 (7–8), 900–910.

Walsh, J., 1965. The effect of cracks on the compressibility of rocks. Journal of Geophysical Research 70, 381–389.

Wong, T.-F., 1982. Micromechanics of faulting in westerly granite. International Journal of Rock Mechanics and Mining Sciences 19, 49–64.

Wu, X., Baud, P., Wong, T.-F., 2000. Micromechanics of compressive failure and spatial evolution of anistropic damage in darley dale sandstone. International Journal of Rock Mechanics and Mining Sciences 37, 143–160.

Zang, A., Wagner, F., Stanchits, S., Janssen, C., Dresen, G., 2000. Fracture process zone in granite. Journal of Geophysical Research 105, 23651–23661.

Zhu, W., Vinciguerra, S., Baud, P., Wong, T.-F., Cavallo, A., 2007. Dilatancy and failure in basalt from Mt Etna under triaxial compression. Geophysical Research Abstracts 9 EGU2007–A–02037.

Zhu, W., Wong, T.-F., 1999. Network modeling of the evolution of permeability and dilatancy in compact rock. Journal of Geophysical Research 104, 2963–2971.

Please cite this article as: Fortin, J., et al., Influence of thermal and mechanical cracks on permeability and elastic wave velocities in a basalt from Mt. Etna volcano subjected to elevated pressure, Tectonophysics (2010), doi:10.1016/j.tecto.2010.09.028